

**MULTIPLE CURRENT DIPOLE ESTIMATION
IN A REALISTIC HEAD MODEL USING
SIGNAL SUBSPACE METHODS**

By

BHAVANA KATYAL

A thesis submitted in partial fulfillment of the
requirements for the degree of

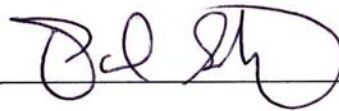
MASTER OF SCIENCE

WASHINGTON STATE UNIVERSITY
School of Electrical Engineering and
Computer Science

AUGUST 2004

To the Faculty of Washington State University:

The members of the Committee appointed to examine the thesis of BHAVANA KATYAL find it satisfactory and recommend that it be accepted.



Chair



ACKNOWLEDGMENTS

With deepest gratitude, I would like to thank my advisor Dr. Paul Schimpf for being a wonderful guide and great teacher. Without his encouragement and guidance, this work would not have been possible. I am grateful for our long discussion on several unanswered issues and his constructive criticism related to this work. I thank him not only for his support on the professional level but for his valuable advise on several personal issues as well. I consider myself lucky to be his student. I would also like to thank Dr. Mortz and Dr. Schneider for their helpful comments on several issues related to this research.

MULTIPLE CURRENT DIPOLE ESTIMATION
IN A REALISTIC HEAD MODEL USING
SIGNAL SUBSPACE METHODS

ABSTRACT

By Bhavana Katyal, M.S.
Washington State University
August 2004

Chair: Paul H. Schimpf

Neural activity in the human brain can be modeled as a volume conductor with current dipoles representing collections of neuronal sources. Determining the spatio-temporal characteristics of the sources from such models requires a solution to the inverse electrostatic problem. In this study, algorithms, R-MUSIC and RAP-MUSIC, based on a signal subspace method, were used to invert combinations of synchronous and asynchronous dipolar sources in an anatomically realistic head model. The source localization of the algorithms was analyzed at signal-to-noise ratios from 0 to 30 dB, for a set of rank-four source configurations. Both the algorithms have the same performance for

all the configurations. Localization of independent sources was excellent, even at low signal-to-noise ratios, demonstrating the potential performance advantages of a spatio-temporal analysis over a purely spatial treatment. The algorithms use a correlation threshold below which it searches for synchronous sources. A fixed correlation threshold was found to be inadequate. A SNR dependent correlation threshold was estimated for a set of rank four configurations considered and performance of the algorithms was analyzed. Localization for configurations containing synchronous sources was substantially degraded at signal-to-noise ratios below 20 dB, demonstrating a need for improved methods to distinguish between asynchronous and synchronous sources. The performance was also observed for a pair of sources of equal power with correlation coefficient of 0, 0.2463, 0.5064, 0.7505, and 1.0 between them. The performance was very good above 10 dB for partially correlated sources. The algorithms are able to identify the independent portion of the time series can be used for source localization of partially correlated sources at higher SNRs. The computational complexity of multidimensional search for synchronous sources was successfully reduced by initially searching the pair of synchronous sources at a lower resolution cortical region. The solution was then found by directing the search to a locally constrained region at full resolution around the initial solution, without degrading the performance.

TABLE OF CONTENTS

ACKNOWLEDGMENTS	III
ABSTRACT.....	IV
LIST OF FIGURES.....	VII
CHAPTER	
1 INTRODUCTION	1
2 THEORY	5
Inverse Electrostatic Problem.....	5
Source Model	9
Signal Subspace.....	11
3 METHODOLOGY	15
Inverse Methods	15
Lead Field Matrix and Head Model	20
Source Model and Performance Metric	22
4 RESULTS AND DISCUSSION.....	26
Correlation Threshold	26
Source Localization.....	37
5 CONCLUSIONS	50
REFERENCES	52

LIST OF FIGURES

Figure 2.1 Location of source and observation point in the given head volume.	7
Figure 2.2 Geometric interpretation of principal angles between matrix A and a line vector B . A is a 2-D plane spanned by 2 vectors A ₁ and A ₂ . Principal angle between A and B . is φ_1 Subspace correlation is given by $\cos(\varphi_1)$. The principal vector in the plane is a_1 and in the line is b_1	13
Figure 3.1 Algorithm used for this study for R-MUSIC and RAP-MUSIC. Metric used for algorithms are given in Eq. 3.3 and 3.5.....	19
Figure 3.2 Iso-surface of modeled domain with cutaway illustrating classified tissues and 145 lead EEG superimposed.....	21
Figure 3.3 Candidate cortical sources.....	21
Figure 3.4 Overlay of 145 EEG channels with 4 dipolar sources (1 rotating in a plane, 1 with a fixed orientation, and 2 synchronous). SNR = 20 dB.....	24
Figure 4.1 Estimate of SNR for Configuration 1 based on estimate of signal norm obtained from the 1 st singular value of signal.....	28
Figure 4.2 Estimate of SNR for Configuration 2 based on estimate of signal norm obtained from the 1 st singular value of signal.....	28
Figure 4.3 Estimate of SNR for Configuration 3 based on estimate of signal norm obtained from the 1 st singular value of signal.....	29
Figure 4.4 Estimate of SNR for Configuration 4 based on estimate of signal norm obtained from the 1 st singular value of signal.....	29
Figure 4.5 Estimated SNR (SNR_{est}) from equation (4.2) for Configuration 1.....	30
Figure 4.6 Estimated SNR (SNR_{est}) from equation (4.2) for Configuration 2.....	30
Figure 4.7 Estimated SNR (SNR_{est}) from equation (4.2) for Configuration 3.....	31
Figure 4.8 Estimated SNR (SNR_{est}) from equation (4.2) for Configuration 4.....	31

Figure 4.9 Subspace correlations for 3 rd and 4 th single-source ITs for Configuration 1 generated by R-MUSIC, with empirical correlation threshold. For comparison, correlation in (4.1) and threshold proposed by Mosher is also shown.	33
Figure 4.10 Subspace correlations for 3 rd and 4 th single-source ITs for Configuration 2 generated by R-MUSIC, with empirical correlation threshold. For comparison, correlation in (4.1) and threshold proposed by Mosher is also shown.	33
Figure 4.11 Subspace correlations for 4 th single-source ITs for Configuration 3 generated by R-MUSIC, with empirical correlation threshold. For comparison, correlation in (4.1) and threshold proposed by Mosher is also shown.	34
Figure 4.12 Subspace correlations for 4 th single-source ITs for Configuration 4 generated by R-MUSIC, with empirical correlation threshold. For comparison, correlation in (4.1) and threshold proposed by Mosher is also shown.	34
Figure 4.13 Subspace correlations for 3 rd and 4 th single-source ITs for Configuration 1 generated by RAP-MUSIC, with empirical correlation threshold. For comparison, correlation in (4.1) and threshold proposed by Mosher is also shown.	35
Figure 4.14 Subspace correlations for 3 rd and 4 th single-source ITs for Configuration 2 generated by RAP-MUSIC, with empirical correlation threshold. For comparison, correlation in (4.1) and threshold proposed by Mosher is also shown.	35
Figure 4.15 Subspace correlations for 4 th single-source ITs for Configuration 3 generated by RAP-MUSIC, with empirical correlation threshold. For comparison, correlation in (4.1) and threshold proposed by Mosher is also shown.	36
Figure 4.16 Subspace correlations for 4 th single-source ITs for Configuration 4 generated by RAP-MUSIC, with empirical correlation threshold. For comparison, correlation in (4.1) and threshold proposed by Mosher is also shown.	36
Figure 4.17 Localization error for 1 independent and 1 rotating source vs. best possible localization of a single source using spatial-only inverse for R-MUSIC.	38
Figure 4.18 Localization error for 1 independent and 1 rotating source vs. best possible localization of a single source using spatial-only inverse for RAP-MUSIC.	38
Figure 4.19 Localization error for source Configurations 1-4 using the empirical correlation threshold (see Eq. 4.3), generated using R-MUSIC.	39
Figure 4.20 Localization error for source Configurations 1-4 using the empirical correlation threshold (see Eq. 4.3), generated using RAP-MUSIC.	39

Figure 4.21 Localization error for source Configuration 1 using the empirical correlation threshold (Eq. 4.3) for R-MUSIC and RAP-MUSIC.....	41
Figure 4.22 Localization error for source Configuration 2 using the empirical correlation threshold (Eq. 4.3) for R-MUSIC and RAP-MUSIC.....	41
Figure 4.23 Localization error for source Configuration 3 using the empirical correlation threshold (Eq. 4.3) for R-MUSIC and RAP-MUSIC.....	42
Figure 4.24 Localization error for source Configuration 4 using the empirical correlation threshold (Eq. 4.3) for R-MUSIC and RAP-MUSIC.....	42
Figure 4.25 Localization error for source Configuration 1 generated using R-MUSIC.	43
Figure 4.26 Localization error for source Configuration 2 generated using R-MUSIC.	43
Figure 4.27 Localization error for source Configuration 3 generated using R-MUSIC.	44
Figure 4.28 Localization error for source Configuration 4 generated using R-MUSIC.	44
Figure 4.29 Localization error for source Configuration 1 generated using RAP-MUSIC.	45
Figure 4.30 Localization error for source Configuration 2 generated using RAP-MUSIC.	45
Figure 4.31 Localization error for source Configuration 3 generated using RAP-MUSIC.	46
Figure 4.32 Localization error for source Configuration 4 generated using RAP-MUSIC.	46
Figure 4.33 Localization error for two sources of equal power with 0%, 24.63%,50.64%, 75.05 and 100% correlation generated using R-MUSIC.	49
Figure 4.34 Localization error for two sources of equal power with 0%, 24.63%,50.64%, 75.05% and 100% correlation generated using RAP-MUSIC.....	49

Chapter 1

INTRODUCTION

Electroencephalography (EEG) is a noninvasive technique to study human brain activity. This technique measures the potential difference between various locations on the scalp. Neural activity in the human brain is modeled as multiple current dipoles. The objective is to estimate a set of current dipoles based on noisy potential measurements from EEG on the scalp. This requires a solution of the inverse electrostatic problem. The inverse problem is inherently ill-posed and has no unique solution. Solutions to these problems are highly based on estimation methods for source parameters such as location, orientation, and total number of sources.

The simplest model is a single dipole in a spherical sphere representing the human head [1]. A single dipole model is an oversimplified model and cannot characterize higher brain activity [2]. A better representation for complex brain functions are multiple dipole models. The human brain is made up of different tissues with varying electrical conductivity. A spherical assumption cannot account for variation in electrical conductivities in the human head [3]. Thus, it is essential to have a realistic head model for

source parameter estimation. Complex head geometries with varying electrical conductivity in different parts of the head can be effectively handled by the finite-element method (FEM) and finite-difference method (FDM) [4].

The solution to inverse electrostatic problems requires a) specification of the model b) specification of the criteria for estimation and c) estimation of parameters. A common approach for the solution is norm-minimization of the solution vector. A least-squares (LS) approach would minimize the residual norm between the estimated and actual measurements of potential. This leads to multiple solutions. A typical approach is to choose the solution with minimum norm, or some weighted norm. Because of nonlinear relationship between measurements and location of the sources, in general, this search must be exhaustive, with a search time that grows as the factorial of the number of dipoles. Therefore, the search for optimum source parameters is nonlinear and multidimensional.

Neuronal activities in a human brain are non-stationary. Initial models used EEG measurements for a single time instant. These models are referred to as ‘instantaneous state dipole’ models [5]. Temporal information can play an important role in analyzing and characterizing EEG and algorithms have been introduced to handle time-frequency analysis [6]. The *multiple signal classification* (MUSIC) algorithm, a signal subspace method, proposed by Schmidt [7] avoids multidimensional search. This algorithm was adapted by

Mosher *etal.* [8] for spatio-temporal model of the source space and later extended to recursive applications (R-MUSIC and RAP-MUSIC) [9] [10].

These recursive algorithms use spatio-temporal *independent topography* (IT) model of the source space described in detail in Chapter 2. When the sources are independent, these algorithms avoid multi-dimensional search by scanning a single source at a time at each node in the three-dimensional (3-D) head model. The location of the source that gives the best projection onto the signal subspace is added to the model. The algorithm first searches for all asynchronously activated dipoles and then synchronously activated dipoles. The algorithms use a correlation threshold below which it searches for synchronous dipoles. When the sources are synchronous, a multidimensional search is still required.

There are two problems that are not explicitly addressed by R-MUSIC and RAP-MUSIC: (i) how to establish a correlation threshold for scanning multi-source ITs, and (ii) how to deal with the factorial increase in computational complexity of synchronous, multi-source, ITs. The first problem is dependent on signal-to-noise ratio (SNR), whereas the second problem is independent of SNR. The feasibility of these recursive algorithms has not been studied for a realistic head model and a wide range of signal-to-noise ratios. In this study, R-MUSIC and RAP-MUSIC methods for multi-dipole models for a realistic head model are of interest. The efficacy of one set of approaches to the above mentioned problems in a realistic head model is examined in this study.

In Chapter 2, the inverse electrostatic problem is developed by Lead Field matrix approach for spatio-temporal model. This chapter also discusses the multi-dipole IT model used for the study and principals of signal subspace methods In Chapter 3, simulation methods and techniques for source localization from the model are discussed. A detailed analysis and discussion of the results obtained from the study is given in Chapter 4. The conclusions drawn from this study are presented in Chapter 5.

Chapter 2

THEORY

Inverse Electrostatic Problem

This work addresses the localization of the neural currents in the brain from the electroencephalogram (EEG). EEG measures the scalp potential in response to a sensory stimulus. Particular interest is in the effectiveness of signal subspace models for a realistic head model. The focus of this study is location of sources at various signal-to-noise ratios for of EEG data.

The neural currents can be modeled as a set of current dipoles representing sources in the brain. The human head can be modeled as a volume conductor. The conductivities of the brain tissue can be obtained from medical imagery and are assumed piecewise constant over the entire domain of head. This reduces the problem to a set of current dipoles in a conducting domain. The relationship between neural current sources and scalp potential is

governed by quasi-static approximation of Maxwell's equations [11], as expressed by the Poisson equation:

$$\nabla \cdot \boldsymbol{\sigma} \nabla \mathbf{V} = -\nabla \cdot \mathbf{J} = -J_V \quad (2.1)$$

where $\boldsymbol{\sigma}$ is the conductivity of the volume V of the domain, \mathbf{V} is the electric potential, \mathbf{J} is the current density and J_V is the volume current density. Determination of source locations from partial observation of the potential field is identified as the Inverse Electrostatic Problem.

The problem formulation starts with the ‘‘Principle of Superposition,’’ which states that a voltage at any location that results from multiple sources is the sum of voltages obtained from each source acting alone. Measurements are linearly dependent on dipole moments [8]. The potential measurement $v(\mathbf{r})$, at location \mathbf{r} can therefore be expressed as:

$$v(\mathbf{r}) = \int_V \mathbf{l}(\mathbf{r}, \mathbf{r}') \cdot \mathbf{j}(\mathbf{r}') d\mathbf{r}' \quad (2.2)$$

where V is the volume of modeled domain, $\mathbf{j}(\mathbf{r}')$ is the current density at any point \mathbf{r}' in the volume, and \mathbf{l} is the Lead Field vector. The Lead Field vector represents a contribution to the potential field at \mathbf{r} from a unit source at a particular location, \mathbf{r}' , and orientation in the volume. To model dipolar current sources, we assume the source exist only at a discrete point \mathbf{r}_q . Figure 2.1 illustrates a dipole current at location \mathbf{r}_q . Now the current density can be written as $\mathbf{j}(\mathbf{r}')\delta(\mathbf{r}' - \mathbf{r}_q)$, where $\delta(\mathbf{r}' - \mathbf{r}_q)$ is the Dirac delta function. Substituting in (2.2) and simplifying gives:

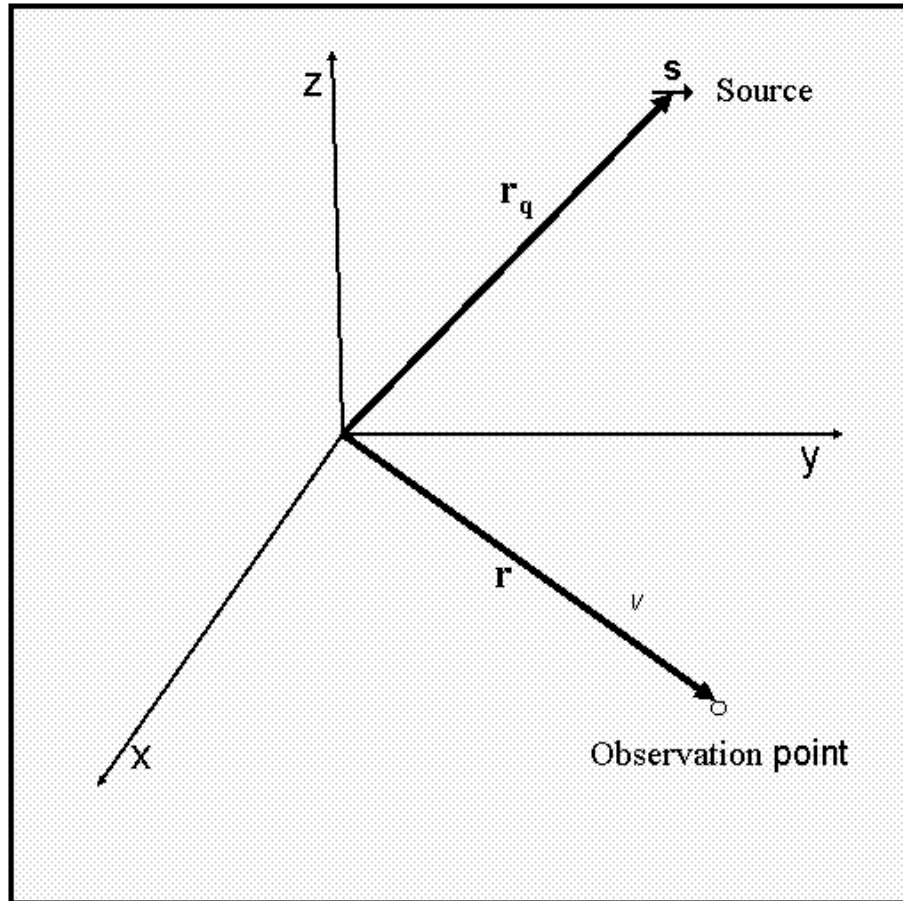


Figure 2.1 Location of source and observation point in the given head volume.

$$\mathbf{v}(\mathbf{r}) = \mathbf{L}(\mathbf{r}, \mathbf{r}_q) \cdot \mathbf{s} \quad (2.3)$$

where, \mathbf{s} is the moment of a current dipole located at \mathbf{r}_q

For a generalized problem with p current dipoles and m potential measurement points for n time instances, equation (2.3) can be expressed as an $m \times n$ spatio-temporal matrix:

$$\begin{bmatrix} v(\mathbf{r}_1, \mathbf{t}_1) & \cdots & v(\mathbf{r}_1, \mathbf{t}_n) \\ \vdots & \ddots & \vdots \\ v(\mathbf{r}_m, \mathbf{t}_1) & \cdots & v(\mathbf{r}_m, \mathbf{t}_n) \end{bmatrix} = \begin{bmatrix} \mathbf{L}(\mathbf{r}_1, \mathbf{r}_{q1}) & \cdots & \mathbf{L}(\mathbf{r}_1, \mathbf{r}_{qp}) \\ \vdots & \ddots & \vdots \\ \mathbf{L}(\mathbf{r}_m, \mathbf{r}_{q1}) & \cdots & \mathbf{L}(\mathbf{r}_m, \mathbf{r}_{qp}) \end{bmatrix} \begin{bmatrix} \mathbf{s}_1(t_1) & \cdots & \mathbf{s}_1(t_n) \\ \vdots & \ddots & \vdots \\ \mathbf{s}_p(t_1) & \cdots & \mathbf{s}_p(t_n) \end{bmatrix} \quad (2.4a)$$

In matrix notation, the above equation can be written as:

$$\mathbf{V}(t) = [\mathbf{L}(\mathbf{r}_{q1}) \quad \cdots \quad \mathbf{L}(\mathbf{r}_{qp})] \mathbf{S}(t) = \mathbf{L}(\mathbf{r}_q) \mathbf{S}(t) \quad (2.4b)$$

Here, $\mathbf{L}(\mathbf{r}_{qi})_{m \times 3}$ is the Lead Field matrix for a dipole located at \mathbf{r}_{qi} and represents the forward field generated by a unit dipole at m sensor locations. Each dipole is associated with a time series represented by rows of \mathbf{S} . For a dipole with invariant location and moment orientation (fixed dipole), the orientation can be separated out from the dipole moments as, $\mathbf{s}_i = \mathbf{u}_{qi} m_{qi}(t_k)$, where \mathbf{u}_{qi} is a unit norm orientation vector for dipole i at location \mathbf{r}_q , and $m_{qi}(t_k)$ is the scalar moment intensity at time index k . Using this assumption (2.4) can be rewritten as:

$$\mathbf{V}(t) = [\mathbf{L}(\mathbf{r}_{q1}) \quad \cdots \quad \mathbf{L}(\mathbf{r}_{qp})] \begin{bmatrix} \mathbf{u}_{q1} & & 0 \\ & \ddots & \\ 0 & & \mathbf{u}_{qp} \end{bmatrix} \cdot \begin{bmatrix} m_{q1}(t_1) & \cdots & m_{q1}(t_n) \\ \vdots & \ddots & \vdots \\ m_{qp}(t_1) & \cdots & m_{qp}(t_n) \end{bmatrix} \quad (2.5a)$$

or

$$\mathbf{V}(t) = \mathbf{L}\mathbf{u} \cdot \mathbf{M} = \mathbf{A}(\mathbf{r}, \mathbf{u})\mathbf{M} \quad (2.5b)$$

$\mathbf{A}(\mathbf{r}, \mathbf{u})$, the gain matrix, has both the time invariant location and moment orientation parameters and each column represents the gain of one complete dipole. For a given (\mathbf{r}, \mathbf{u}) , the above equation can be solved for \mathbf{M} . Based on the number of measurements, m , and number of dipoles, p , there can be three possibilities: $m = p$, exact solution; $m > p$, over determined problem; $m < p$, under determined problem with no unique solution. For this study, the case of $(m > p)$ was considered.

Source Model

To explore the problem, it is essential to describe the dipole model. Based on the location and orientation, a dipole can be characterized either ‘fixed’ or ‘rotating’. A dipole fixed in location and orientation in space is termed ‘fixed dipole’. A ‘rotating dipole’ has fixed location but unconstrained orientation in space. The time dependence of the dipole moment leads to asynchronous and synchronous dipoles. Asynchronous dipoles have independent time series associated with them, whereas synchronous dipoles have a single time series.

A source model based on Independent Topography (IT) can be defined. An IT is defined as one or more nonrotating dipoles with a single time series, and for this work, termed as a ‘single source’. Each IT has an independent combination of location parameter and time series than other ITs. A single IT may comprise more than one spatially distinct source with a synchronous activation. A ‘rotating’ source is modeled as multiple ITs, with the same location but independent time series. In this framework, p dipoles can be grouped into r subsets, each representing an IT. Under these conditions, (2.4b) can be rewritten as:

$$\mathbf{V}(t) = [\mathbf{L}(\boldsymbol{\rho}_1) \ \cdots \ \mathbf{L}(\boldsymbol{\rho}_r)]\mathbf{S}(t) = \mathbf{L}(\boldsymbol{\rho})\mathbf{S}(t) \quad (2.6)$$

where $\boldsymbol{\rho}_i \equiv [\mathbf{r}_{q_1}^{(i)}, \dots, \mathbf{r}_{qp_i}^{(i)}]$ is the location parameters of p_i dipoles of the i^{th} IT. As in (2.5), orientation can be separated from moments of each IT [9] and (2.6) can be reduced as:

$$\mathbf{V}(t) = \mathbf{L}(\boldsymbol{\rho})\mathbf{S} = [\mathbf{a}(\boldsymbol{\rho}_1, \mathbf{u}_1) \ \cdots \ \mathbf{a}(\boldsymbol{\rho}_r, \mathbf{u}_r)] \begin{bmatrix} m_1 \\ \vdots \\ m_r \end{bmatrix} = \mathbf{A}(\boldsymbol{\rho}, \mathbf{u})\mathbf{M} \quad (2.7)$$

where $\mathbf{u} = [\mathbf{u}_1, \dots, \mathbf{u}_r]$ are the unit norm orientation vectors for r ITs. Here, the orientation vector is generalized to include the orientation of all the dipoles in an IT. Under these conditions, \mathbf{V} is of rank r , forcing both $\mathbf{A}(\boldsymbol{\rho}, \mathbf{u})$ and \mathbf{M} to be of full column rank of r . In this spatio-temporal model, the number of sources is equal to the rank of the model. The case where all dipoles are fixed and synchronous results in rank one and the case where all p dipoles rotate in three dimensions and are asynchronous, yields a rank of $3p$.

Signal Subspace

The above model is for noiseless data. In the real world, the measurements are corrupted by noise. Thus, equation (2.7) can be extended to include additive noise $\mathbf{N}(t)$ as given by:

$$\mathbf{V}(t) = \mathbf{A}\mathbf{M}^T + \mathbf{N}(t) \quad (2.8)$$

It is assumed that the noise added is zero mean and white. Under these assumptions, the expected outer product of the noisy signal is:

$$\mathbf{R}_v = E\{\mathbf{v}\mathbf{v}^T\} = \mathbf{A}\mathbf{M}^T\mathbf{M}\mathbf{A}^T + n\sigma_e^2\mathbf{I} \quad (2.9)$$

where \mathbf{R}_v is the autocorrelation matrix of the data, $E\{\cdot\}$ is the expectation operator, σ_e^2 is the covariance of noise signal and \mathbf{I} is the identity matrix. By assumption, $\mathbf{A}\mathbf{M}^T\mathbf{M}\mathbf{A}^T$ is square symmetric with rank r , and its eigen-decomposition is $(\mathbf{\Phi}_s\mathbf{\Lambda}\mathbf{\Phi}_s^T)$. Here, $\mathbf{\Phi}_s$ is a matrix of $m \times r$ eigenvectors and $\mathbf{\Lambda}$ is $r \times r$ diagonal matrix of nonzero eigenvalues. Rank r is equal to the number of ITs in the model. Also, $\text{span}(\mathbf{\Phi}_s) = \text{span}(\mathbf{A})$. Similarly $(n\sigma_e^2\mathbf{I})$ can be decomposed as $(\mathbf{\Phi}_e(n\sigma_e^2\mathbf{I})\mathbf{\Phi}_e^T)$, where $\mathbf{\Phi}_e$ contains $m \times m$ eigenvectors of noise and $(n\sigma_e^2\mathbf{I})$ is $m \times m$ corresponding diagonal matrix of eigenvalues. The autocorrelation matrix of the data can now be stated as:

$$\begin{aligned} \mathbf{R}_v &= [\mathbf{\Phi}_s, \mathbf{\Phi}_e] \begin{bmatrix} \mathbf{\Lambda} + n\sigma_e^2\mathbf{I} & 0 \\ 0 & n\sigma_e^2\mathbf{I} \end{bmatrix} [\mathbf{\Phi}_s, \mathbf{\Phi}_e]^T \\ &= \mathbf{\Phi}_s\mathbf{\Lambda}_s\mathbf{\Phi}_s^T + \mathbf{\Phi}_e\mathbf{\Lambda}_e\mathbf{\Phi}_e^T \end{aligned} \quad (2.10)$$

where Λ_s contains r eigenvalues consisting of both the signal and noise eigenvalues, and Λ_e is a matrix of $(m-r)$ noise only eigenvalues. Φ_s and Φ_e contain vectors orthogonal to each other, generating orthogonal subspaces. The ‘Signal’ subspace is defined as $\text{span}(\Phi_s)$, and orthogonal subspace or noise only subspace as $\text{span}(\Phi_e)$. The columns of $\mathbf{A}(\boldsymbol{\rho}, \mathbf{u})$ spans the same dimensional subspace as Φ_s . An estimate of Φ_s can determine the parameters of the model by comparing the estimated subspace ($\hat{\Phi}_s$) to the columns of \mathbf{A} . This forms the basis for Signal Subspace Methods for parameter estimation of the model.

‘Subspace correlation’ is a metric to compare the subspace spanned by \mathbf{A} and $\hat{\Phi}_s$. Each of these matrices can be represented by a set of orthonormal basis vectors termed principal vectors. The geometric angles, $\{\varphi_k\}$, between the basis vectors of the two matrices are called principal angles. Subspace correlation, c_k , is the cosine of the principal angle; $c_k = \cos(\varphi_k)$. Figure 2.2 gives a geometric interpretation of principal angle between a 2-D matrix \mathbf{A} and a vector \mathbf{B} .

If r is the minimum of the rank of the two matrices, r ordered subspace correlations, $(1 \geq c_1 \geq c_2 \geq \dots \geq c_r \geq 0)$, can be obtained. The maximum correlation is given by c_1 and minimum correlation by c_r . If k^{th} subspace correlation approaches one; $c_k = 1$; there are k parallel bases between the subspaces. On the other hand, k^{th} subspace correlation approaching zero, i.e. $c_k = 0$, comprises $(r-k)$ orthogonal bases. For $c_1 = 1$, there is at least a

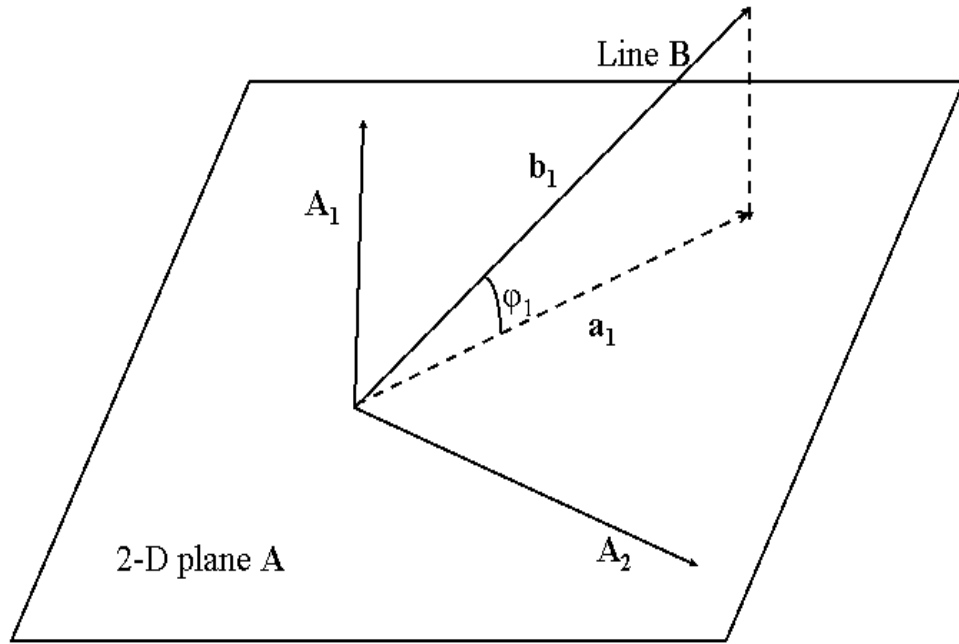


Figure 2.2 Geometric interpretation of principal angles between matrix \mathbf{A} and a line vector \mathbf{B} . \mathbf{A} is a 2-D plane spanned by 2 vectors \mathbf{A}_1 and \mathbf{A}_2 . Principal angle between \mathbf{A} and \mathbf{B} is ϕ_1 . Subspace correlation is given by $\cos(\phi_1)$. The principal vector in the plane is a_1 and in the line is b_1 .

one-dimensional (1-D) subspace in common, and for $c_1 = 0$; the subspaces are orthogonal.

Two subspaces are equivalent or parallel when $\{ c_k \}_{k = 1..r} \rightarrow 1$. Subspace correlation metric is the basis for MUSIC and its variant algorithms, which are addressed in next section.

Chapter 3

METHODOLOGY

Inverse Methods

This section presents a brief description of signal subspace methods considered for this study, R-MUSIC and RAP-MUSIC. The two methods are variants of the MUSIC algorithm given by Moshier *etal.* The MUSIC algorithm is described first and then extended to its variant algorithms.

MUSIC

A detailed description of MUSIC algorithm can be found in [8]. Here, a brief description of the essential elements of the MUSIC algorithm is presented. The MUSIC algorithm finds location and orientation for an IT that maximizes the first subspace correlation, i.e. c_1 . The metric used is given by:

$$c_1^2\{\mathbf{a}(\boldsymbol{\theta}), \hat{\boldsymbol{\Phi}}_s\} = \frac{(\mathbf{a}(\boldsymbol{\theta})^T \hat{\boldsymbol{\Phi}}_s \hat{\boldsymbol{\Phi}}_s^T \mathbf{a}(\boldsymbol{\theta}))}{\|\mathbf{a}(\boldsymbol{\theta})\|^2} \quad (3.1)$$

where $\boldsymbol{\theta} = (\boldsymbol{\rho}, \mathbf{u})$ is the parameter for a source containing both nonlinear location and quasi-linear orientation parameters and $\mathbf{a}(\boldsymbol{\theta})$ has been defined in (2.7). The Lead Field matrix, $\mathbf{L}(\boldsymbol{\rho})$, is nonlinearly dependent on location parameter. The orientation vector, \mathbf{u}_i , creates a linear combination of columns of $\mathbf{L}(\boldsymbol{\rho}_i)$. Therefore, columns $\mathbf{L}(\boldsymbol{\rho}_i)$ which give the maximum subspace correlation, $c_1\{\mathbf{L}(\boldsymbol{\rho}_i), \hat{\boldsymbol{\Phi}}_s\}$, also produce the best orientation vector for the solution. This simplifies the problem and the metric in (3.1) can be rewritten in terms of $\mathbf{L}(\boldsymbol{\rho}_i)$:

$$c_1^2\{\mathbf{L}(\boldsymbol{\rho}), \hat{\boldsymbol{\Phi}}_s\} = \frac{(\mathbf{L}(\boldsymbol{\rho})^T \hat{\boldsymbol{\Phi}}_s \hat{\boldsymbol{\Phi}}_s^T \mathbf{L}(\boldsymbol{\rho}))}{\|\mathbf{L}(\boldsymbol{\rho})\|^2} \quad (3.2)$$

The algorithm spans the entire domain and at every node in the domain calculates the subspace correlation metric, $c_1^2\{\mathbf{L}(\boldsymbol{\rho}_i), \hat{\boldsymbol{\Phi}}_s\}$. The rank, r , of the signal subspace can be estimated by visual or algorithmic methods [8] [12]. Then, locations of r sources for which the metric approaches unity are searched. The orientation vector is computed for these r candidate sources. This simple approach of locating each source separately based on a global metric makes MUSIC computationally attractive as it avoids high dimensional searches as in least-squares methods [13]. In addition, the search is exhaustive over the parameter space and avoids the problems of a solution converging to local minima as in nonconvex optimization techniques [14]. However, there are errors in estimating the signal

subspace and it can be difficult to identify true maximum subspace correlations (peaks). Also, automatically locating peaks in multi-dimensional problem can be difficult. Moreover, the method is not practical for ITs with more than one dipole. For this study, two variants of MUSIC, namely Recursive (R) MUSIC and Recursively Applied and Projected (RAP) MUSIC have been considered.

R-MUSIC

R-MUSIC builds a model of the source space iteratively by scanning for one IT at a time. At any iteration, ITs that have been found make up the current model. At each iteration, i , the measured field (from \mathbf{L}), for each potential IT, is concatenated to the current source model. The IT that maximizes the i^{th} subspace correlation (which is the minimum subspace correlation for the model being considered) is selected as the next component in the source model. The goal is to maximize the ‘minimum subspace correlation’ at any iteration. This can be interpreted as minimizing the distance between the two subspaces. The algorithm first searches for all 1-dipolar ITs, then for 2-dipolar ITs, and continues so forth. When all 1-dipolar ITs have been extracted, at the next iteration, no single dipole location correlates well with the signal subspace. A correlation threshold can be specified to determine how well an IT configuration correlates with the signal. When the correlation metric falls below the threshold, 2-dipolar ITs are searched. For 2-dipolar IT, two dipole locations are searched simultaneously to maximize the correlation metric for that iteration. The procedure is extended similarly for higher order ITs. The number of independent ITs

searched is equal to the rank of the signal subspace. The search can be stopped when the estimated rank is achieved or the residual signal falls below the noise level. The algorithm can be summarized as:

$$\hat{\boldsymbol{\rho}}_i = \arg \max_{\boldsymbol{\rho}} c_i \{ [\hat{\mathbf{A}}_{i-1} \mathbf{L}(\boldsymbol{\rho})], \hat{\boldsymbol{\Phi}}_s \} \quad (3.3)$$

where i is the iteration number, $\hat{\boldsymbol{\rho}}_i$ is the estimated location parameter for iteration i , and $\hat{\mathbf{A}}_{i-1}$ is the estimated model for iteration $(i-1)$.

RAP-MUSIC

RAP-MUSIC is also an iterative algorithm. The search for an IT is performed in the orthogonal signal subspace of the current model. A modified subspace is formed by removing the component of the signal that is spanned by the current model. The IT that maximizes the first subspace correlation for this modified subspace is added to the model. For any iteration, the orthogonal projector (Π_i^\perp) for current model, $\hat{\mathbf{A}}_i$ is:

$$\Pi_i^\perp \equiv \left(\mathbf{I} - \hat{\mathbf{A}}_i (\hat{\mathbf{A}}_i^H \hat{\mathbf{A}}_i)^{-1} \hat{\mathbf{A}}_i^H \right) \quad (3.4)$$

To form the modified subspace for the next iteration, this projector is applied to both the measured field and signal subspace. The next IT is found that maximizes c_1 for this modified subspace and the algorithm can be summarized as:

$$\hat{\boldsymbol{\rho}}_{i+1} = \arg \max_{\boldsymbol{\rho}} c_1 \{ \Pi_i^\perp \mathbf{L}(\boldsymbol{\rho}), \Pi_i^\perp \hat{\boldsymbol{\Phi}}_s \} \quad (3.5)$$

The algorithm for both R-MUSIC and RAP-MUSIC is given in Figure 3.1.

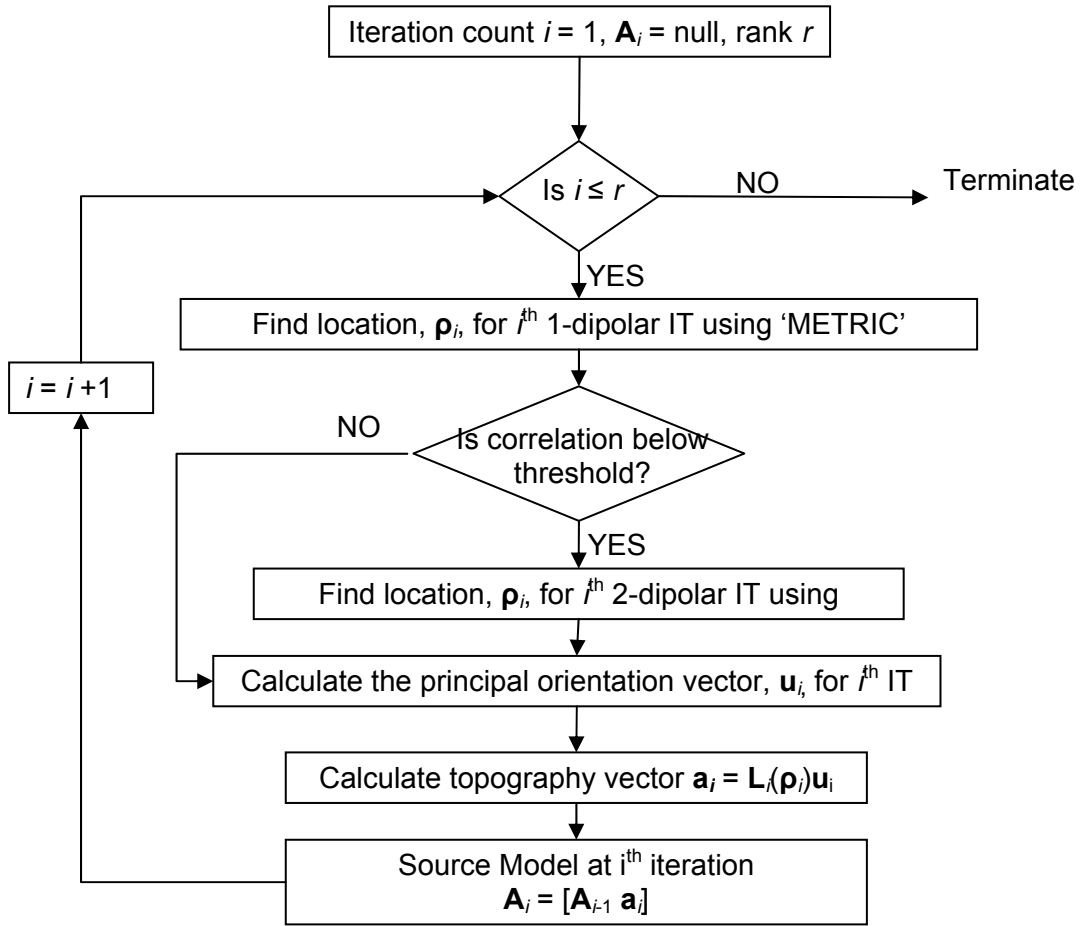


Figure 3.1 Algorithm used for this study for R-MUSIC and RAP-MUSIC. Metric used for algorithms are given in Eq. 3.3 and 3.5

Lead Field Matrix and Head Model

The Lead Field matrix was generated by solving Poisson equation (2.1) using a finite element (FE) method with a realistic representation of the conductor volume based on magnetic resonance (MR) images of a human head [15]. The forward field is generated by solving equation (2.1) for a unit dipole at every cortical node and three orthogonal directions in the volume and is computationally expensive.

MR images of a human head were used to obtain the model domain. The MR images had a resolution of $1.0 \times 1.0 \times 3.2$ mm. The images were classified according to tissue type and averaged to a $2.0 \times 2.0 \times 3.2$ mm resolution [16]. The modeled domain is illustrated in Figure 3.2, overlaid with the 145 lead EEG configuration that was used in this study. A set of 3,035 locations on the surface were taken as potential sources. The average resolution of these locations was 4 mm. These cortical locations are shown in Figure 3.3. At each of these cortical locations, the forward model was solved for a unit dipole oriented in each of the three dimensions. This required 9105 separate finite element runs resulting in 145×9105 column lead-field matrix for the entire domain.

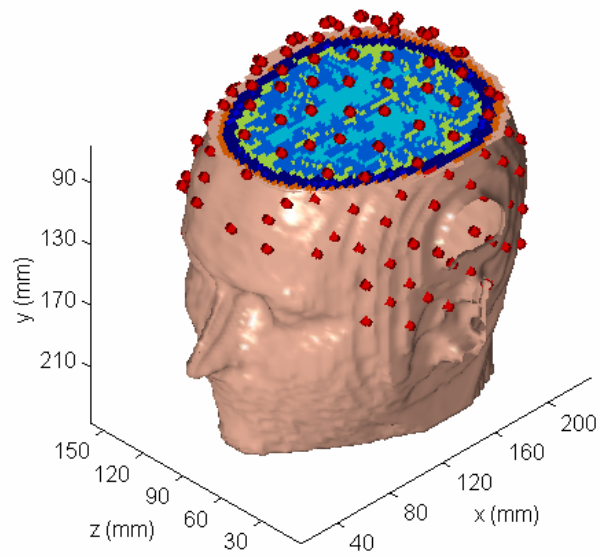


Figure 3.2 Iso-surface of modeled domain with cutaway illustrating classified tissues and 145 lead EEG superimposed.

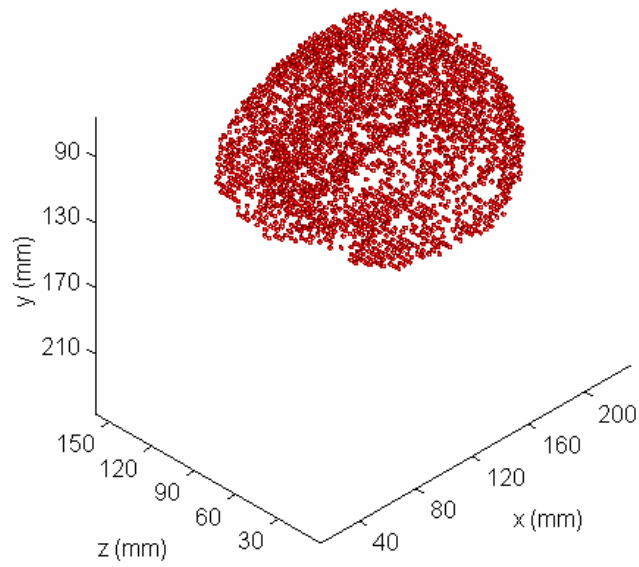


Figure 3.3 Candidate cortical sources.

Source Model and Performance Metric

For the test cases, four configurations of randomly located dipoles with a total of rank four were considered:

- i. *Configuration 1* contained one dipole with a fixed, but randomly generated orientation (rank 1), a second dipole with an independent time-series rotating through 90 degrees in a randomly oriented plane (rank 2), and two synchronous dipoles with time series independent of the others (rank 1).
- ii. *Configuration 2* contained three independent non-rotating sources (rank 3) and one synchronous pair (rank 1).
- iii. *Configuration 3* contained four independent, non-rotating sources (rank 4),
- iv. *Configuration 4* contained two independent sources (rank 2) and one rotating source (rank 2).

Synchronous sources were limited to a complexity of two. Initially the synchronous pair was searched at lower resolution collection of possible cortical sites. The resolution was 10 mm for initial search. Once the best 2-dipolar IT was found, the search was restarted at full resolution of 4 mm for locations falling within 20 mm of the low-resolution pair.

The EEG signal was generated by solving the forward model for each configuration. Uncorrelated Gaussian noise was added to each channel. An example of overlaid EEG signals from all 145 channels for 100 time samples is shown in Figure 3.4.

The performance was examined over SNRs from 0 to 30 dB in 5 dB increments. SNR was defined as:

$$SNR = \frac{\|\mathbf{L}\mathbf{s}(t)\|_F}{\|\mathbf{n}(t)\|_F} \quad (3.6)$$

where subscript F indicates the Frobenius norm. The test cases were run for fifty trials of each randomized source configuration at each SNR. A Performance metric (ε) for source localization was defined as the average spatial location error between the actual (\mathbf{r}_{act}) and inverted sources (\mathbf{r}_{est}), where a rotating source (rank 2) was counted only once and is given by:

$$\varepsilon = \min_{r!} \left\{ \frac{1}{r} \sum_{i=1}^r \|\mathbf{r}_{\text{act}}^i - \mathbf{r}_{\text{est}}^i\| \right\} \quad (3.7)$$

where $r!$ is the number of ways the estimated sources can be matched to actual sources. The configuration that gives the minimum average spatial location is chosen for the performance metric.

For the performance metric, the number of estimated sources was required to be equal to the number of actual sources. In order to ensure that the test cases produced as

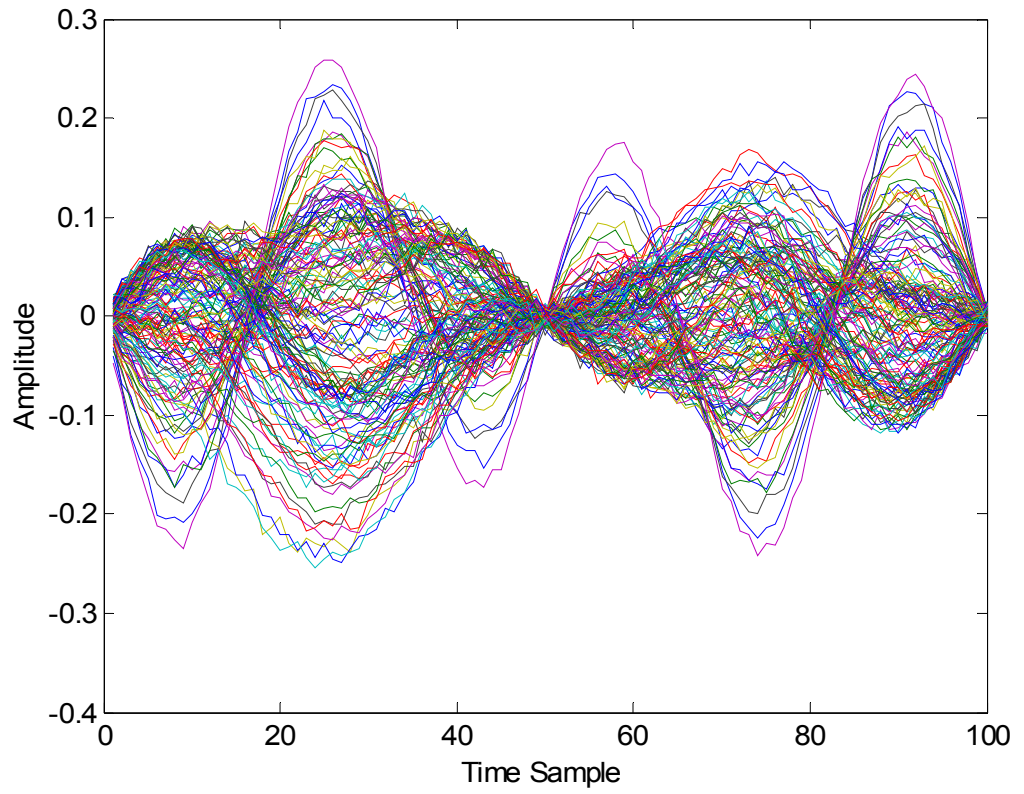


Figure 3.4 Overlay of 145 EEG channels with 4 dipolar sources (1 rotating in a plane, 1 with a fixed orientation, and 2 synchronous). SNR = 20 dB.

many inverted source locations as actual source locations, the rank was over-predicted to be five. The estimated locations were considered regardless of whether the algorithm successfully distinguished between rotating and synchronous sources.

Chapter 4

RESULTS AND DISCUSSION

In this chapter, the performance of source localization simulated by algorithms R-MUSIC and RAP-MUSIC are presented. Performance at SNRs 0-30 dB for Configurations 1-4 (discussed in Chapter 3), was obtained. SNR has been defined in Chapter 3. Fifty trials of each randomized source configuration were run at each SNR.

In the following section, first an attempt has been made to establish a correlation threshold for scanning multi-dipolar ITs. The performance of the algorithms was obtained for the empirical threshold that was considered.

Correlation Threshold

The original description of R-MUSIC [9] suggests a fixed correlation threshold (cc) of 0.95 for multisource ITs. From this study, it was found this threshold is only applicable

for a very restricted range of SNR. A theoretical relationship between the expected model correlation and the SNR may be derived from the standard statistical interpretation of the coefficient of determination, as follows:

$$cc^2 = \frac{\|\mathbf{L}\mathbf{s}\|^2}{\|\mathbf{L}\mathbf{s} + \mathbf{n}\|^2} = \frac{\|\mathbf{L}\mathbf{s}\|^2}{\|\mathbf{L}\mathbf{s}\|^2 + \|\mathbf{n}\|^2} = \frac{\text{SNR}^2}{\text{SNR}^2 + 1} \quad (4.1a)$$

$$\Rightarrow cc = \sqrt{\frac{\text{SNR}_{\text{est}}^2}{\text{SNR}_{\text{est}}^2 + 1}} \quad (4.1b)$$

where SNR_{est} is based on estimates of the signal norm and noise norm. Signal norm was obtained from the first singular value of the signal. It was assumed that an accurate estimate of the noise norm could be obtained from a quiescent, or pre-stimulus, recording. An estimate of SNR obtained from (3.6), is plotted for each configuration in Figures 4.1 – 4.4. In the figures, vertical bars indicate the 95% confidence interval on the mean. As seen from the figures, this estimate gives a good approximation to actual SNR. A correction factor was further applied to this estimate of SNR, which is given by:

$$\text{SNR}_{\text{est}} = 1.0009 \cdot \text{SNR}_{\text{est}}^1 + 1.2577 \quad (4.2)$$

where $\text{SNR}_{\text{est}}^1$ is the estimate of SNR obtained from the first singular value of the signal. In (4.2) both SNR_{est} and $\text{SNR}_{\text{est}}^1$ are in dB. The estimated SNR in (4.2) is plotted in Figures 4.5 – 4.8. This correction factor was determined head model and source configurations considered and may be dependent on the head model. From the figures, it can be observed that SNR_{est} is in very good agreement with actual SNR.

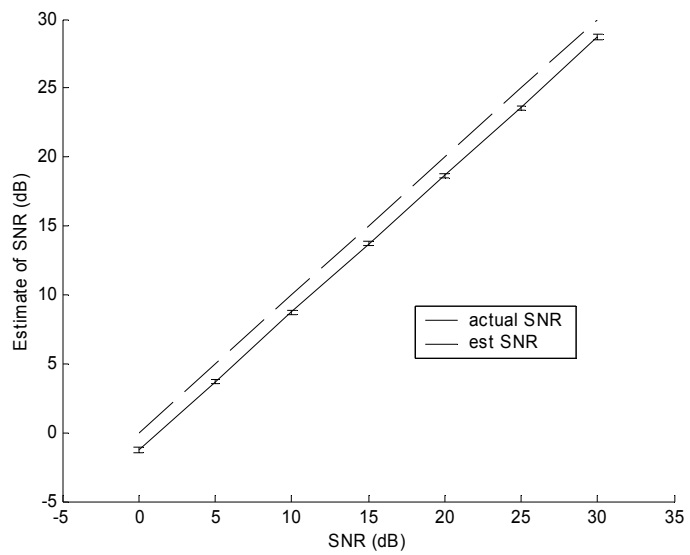


Figure 4.1 Estimate of SNR for Configuration 1 based on estimate of signal norm obtained from the 1st singular value of signal.

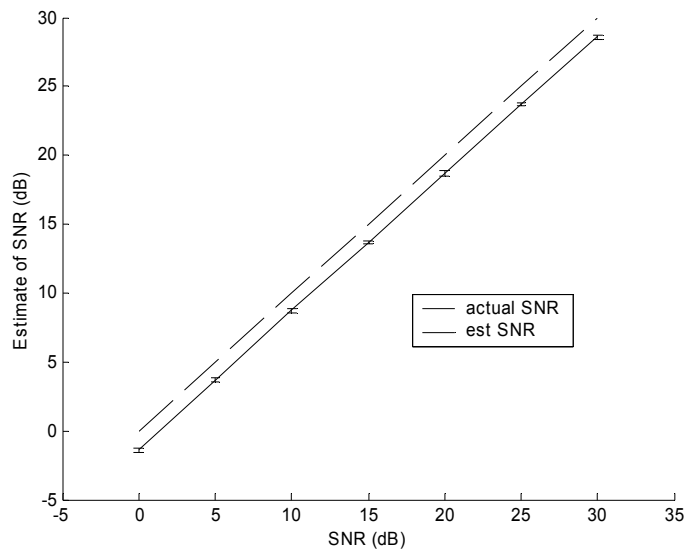


Figure 4.2 Estimate of SNR for Configuration 2 based on estimate of signal norm obtained from the 1st singular value of signal.

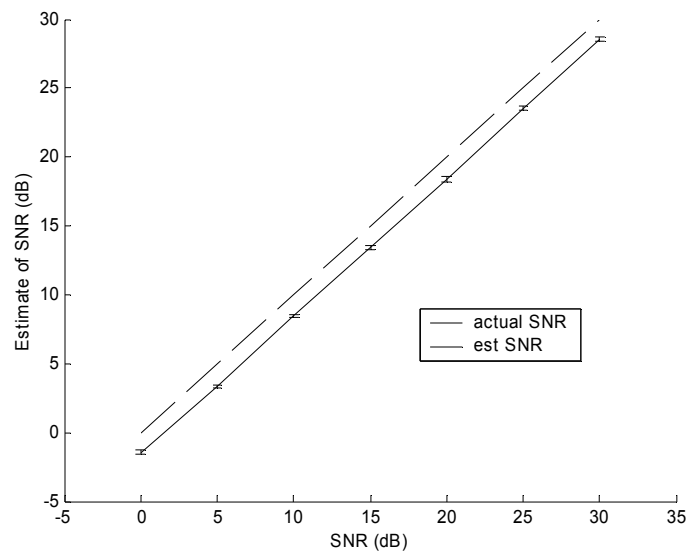


Figure 4.3 Estimate of SNR for Configuration 3 based on estimate of signal norm obtained from the 1st singular value of signal.

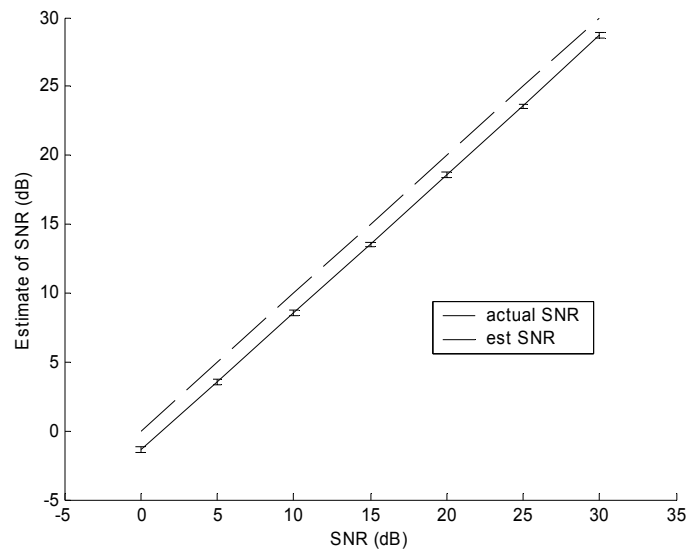


Figure 4.4 Estimate of SNR for Configuration 4 based on estimate of signal norm obtained from the 1st singular value of signal.

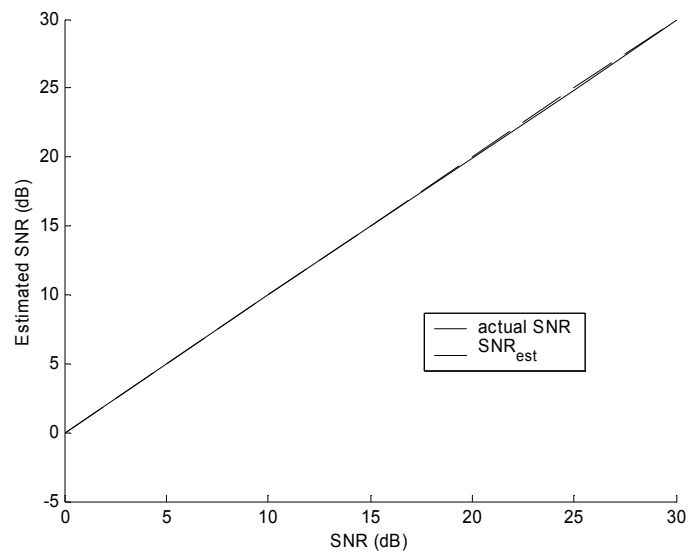


Figure 4.5 Estimated SNR (SNR_{est}) from equation (4.2) for Configuration 1.

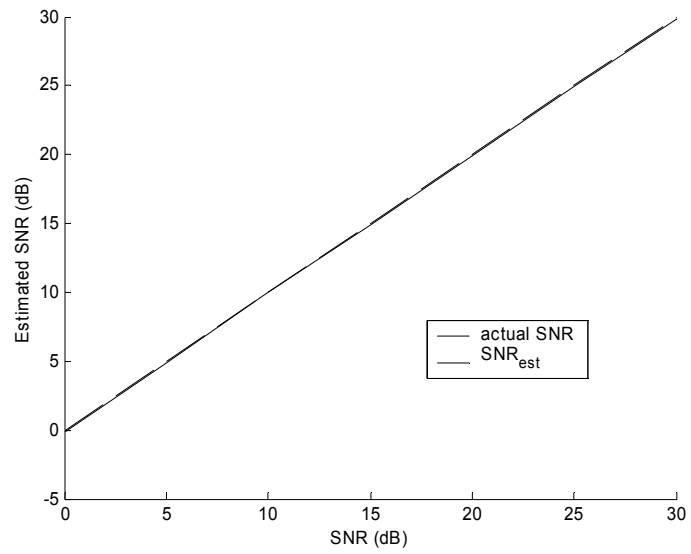


Figure 4.6 Estimated SNR (SNR_{est}) from equation (4.2) for Configuration 2.

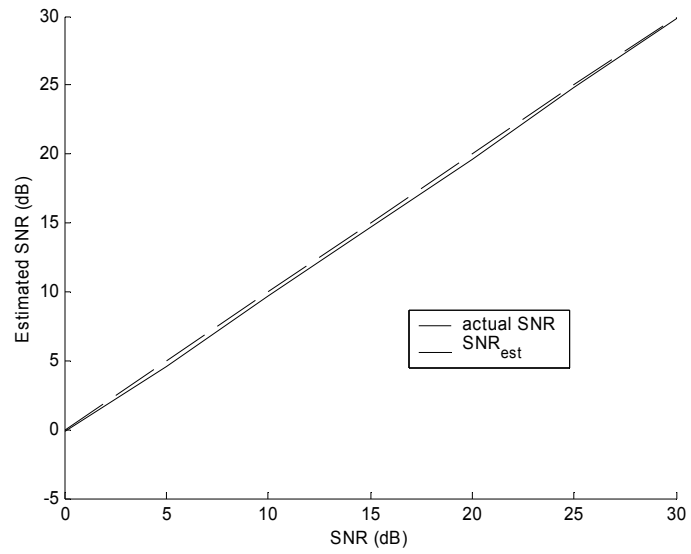


Figure 4.7 Estimated SNR (SNR_{est}) from equation (4.2) for Configuration 3.

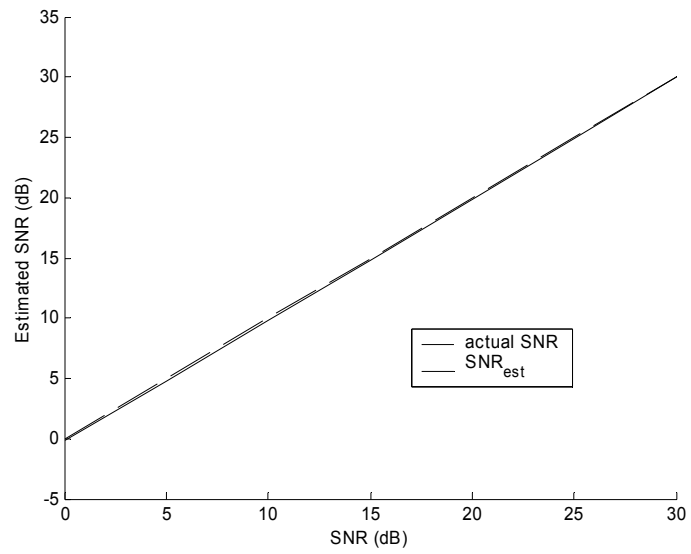


Figure 4.8 Estimated SNR (SNR_{est}) from equation (4.2) for Configuration 4.

Equation (4.1b) establishes a theoretical basis for the correlation threshold. However, in this study, it was found to be inadequate. The threshold given by (4.1) was (i) too high at SNR above 20 dB and (ii) too low at SNRs below 20 dB for source configurations with rank less than four. An empirical adjustment to this threshold was proposed as follows:

$$cc = 0.99 \left(1 - 0.28 \times \text{SNR}_{\text{est}}^{-1.67} \right) \quad (4.3)$$

In order to test the feasibility of a SNR-dependent threshold, the subspace correlations that were obtained for various rank-four source configurations were plotted. A satisfactory correlation threshold would fall below the correlations obtained for independent sources, and above the correlations obtained for matching a single-source IT to synchronous sources. Figures 4.9 – 4.16 illustrate the results for all four configurations for both R-MUSIC and RAP-MUSIC. In the figures, vertical bars indicate the 95% confidence interval on the mean. For Configuration 1 and 2, a satisfactory threshold would fall between the 3rd and 4th single-source ITs. These configurations are plotted in Figures 4.9-4.10 for R-MUSIC and in Figures 4.13-4.14 for RAP-MUSIC. It can be observed that a fixed threshold of 0.95 is not applicable for SNRs above 10 dB. For Configuration 3 and 4, the threshold should fall below the 4th single source IT. These configurations are plotted in Figures 4.11-4.12 for R-MUSIC and Figures 4.15-4.16 for RAP-MUSIC. The threshold is within the confidence interval for SNRs below 15 dB for all four configurations. It is evident that the threshold is highly configuration dependent. The threshold proposed in (4.3) was created as a compromise for all four configurations.

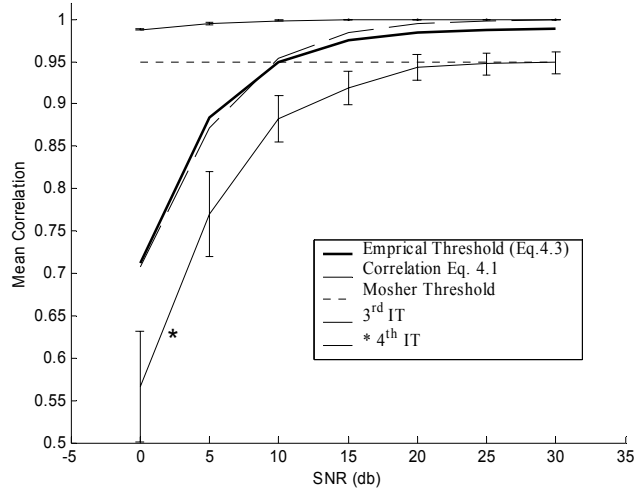


Figure 4.9 Subspace correlations for 3rd and 4th single-source ITs for Configuration 1 generated by R-MUSIC, with empirical correlation threshold. For comparison, correlation in (4.1) and threshold proposed by Mosher is also shown.

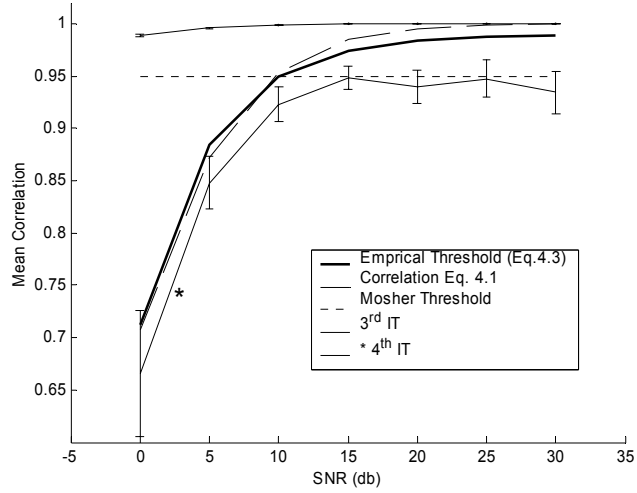


Figure 4.10 Subspace correlations for 3rd and 4th single-source ITs for Configuration 2 generated by R-MUSIC, with empirical correlation threshold. For comparison, correlation in (4.1) and threshold proposed by Mosher is also shown.

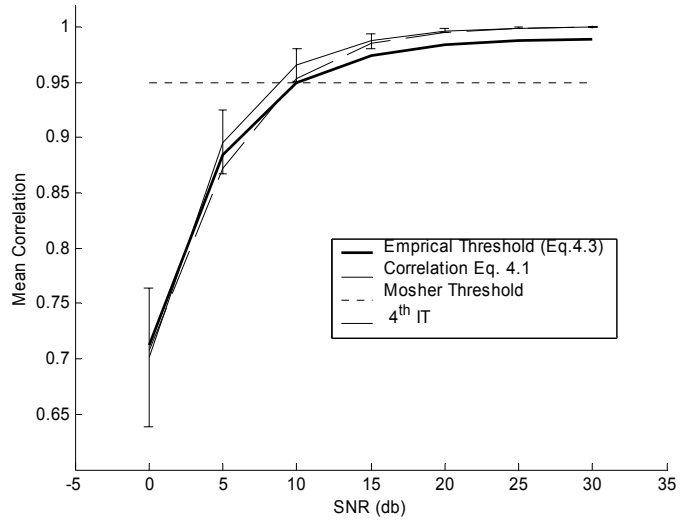


Figure 4.11 Subspace correlations for 4th single-source ITs for Configuration 3 generated by R-MUSIC, with empirical correlation threshold. For comparison, correlation in (4.1) and threshold proposed by Mosher is also shown.

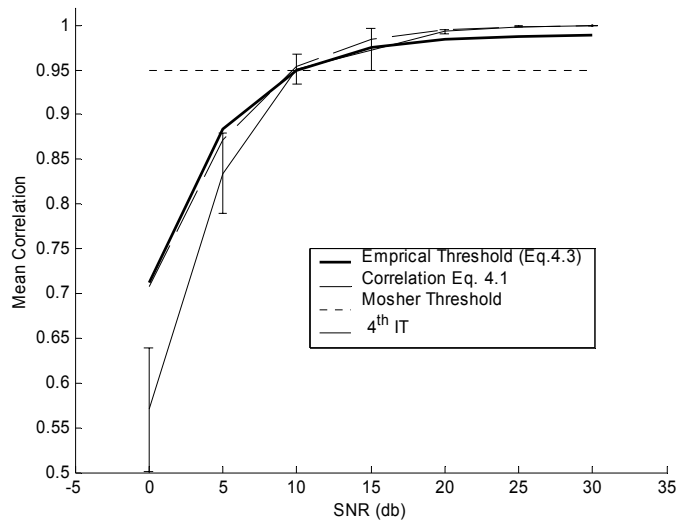


Figure 4.12 Subspace correlations for 4th single-source ITs for Configuration 4 generated by R-MUSIC, with empirical correlation threshold. For comparison, correlation in (4.1) and threshold proposed by Mosher is also shown.

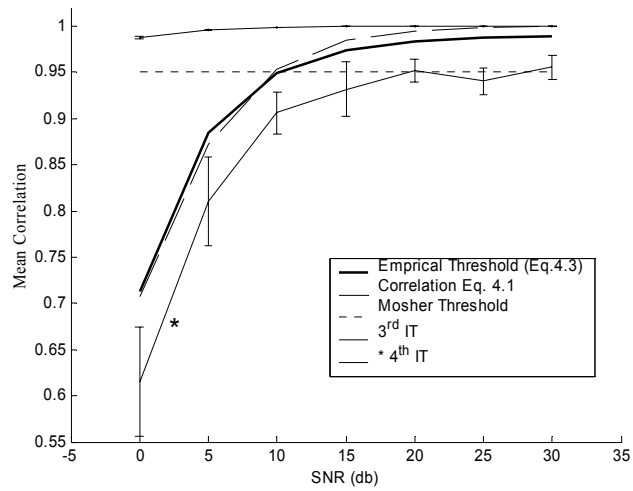


Figure 4.13 Subspace correlations for 3rd and 4th single-source ITs for Configuration 1 generated by RAP-MUSIC, with empirical correlation threshold. For comparison, correlation in (4.1) and threshold proposed by Moshier is also shown.

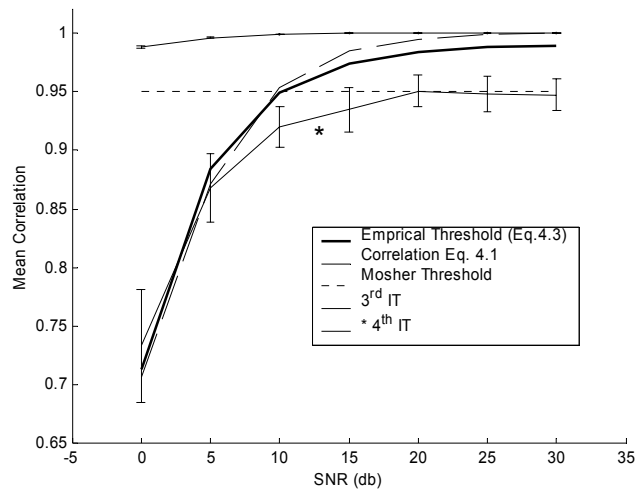


Figure 4.14 Subspace correlations for 3rd and 4th single-source ITs for Configuration 2 generated by RAP-MUSIC, with empirical correlation threshold. For comparison, correlation in (4.1) and threshold proposed by Moshier is also shown.

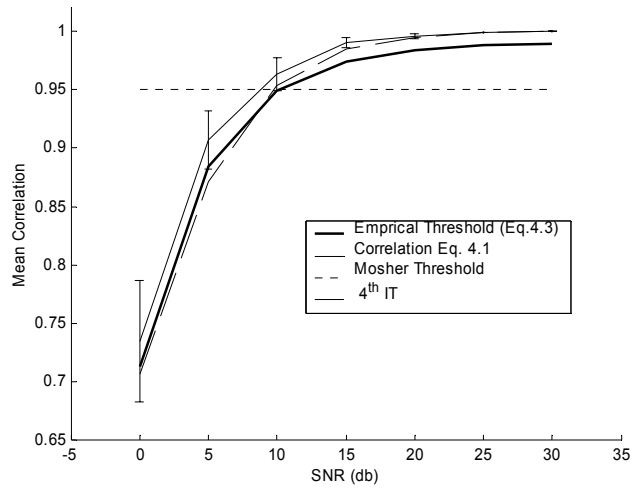


Figure 4.15 Subspace correlations for 4th single-source ITs for Configuration 3 generated by RAP-MUSIC, with empirical correlation threshold. For comparison, correlation in (4.1) and threshold proposed by Mosher is also shown

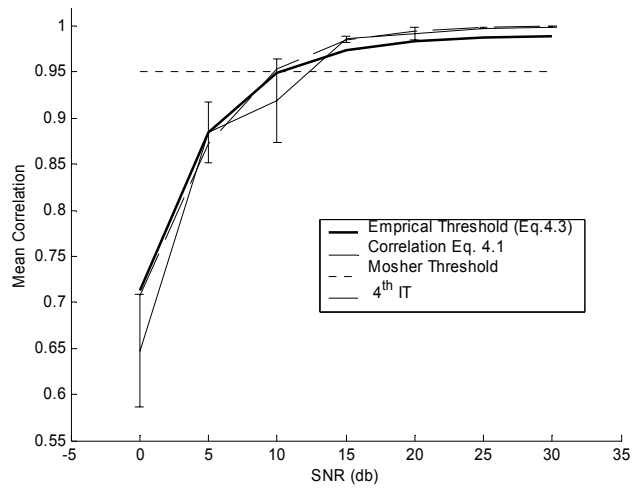


Figure 4.16 Subspace correlations for 4th single-source ITs for Configuration 4 generated by RAP-MUSIC, with empirical correlation threshold. For comparison, correlation in (4.1) and threshold proposed by Mosher is also shown.

Source Localization

To see the benefits of temporal information on source localization both the algorithms, R-MUSIC and RAP-MUSIC, were restricted to scan only for 1-dipolar ITs. Figures 4.17-4.18 shows the mean location error metric vs. SNR for the case where the actual sources contained only asynchronous dipoles, one independent dipole and one rotating dipole, with random locations and orientations. Vertical bars indicate the 95% confidence interval on the mean. For purposes of comparison, these figures also show the best possible localization of a single dipole using only spatial information [17]. These figures show that by exploiting temporal information can dramatically improve source localization for asynchronous sources.

Figures 4.19-4.20 illustrate the localization performance for each of the four source configurations using the empirical correlation threshold in (4.3) for R-MUSIC and RAP-MUSIC. In comparison to Figures 4.17-4.18, the localization performance is still relatively good for configurations 3 and 4, which contain only asynchronous sources. The performance for Configurations 1 and 2 are degraded by the presence of synchronous sources. An analysis of the data shows that the primary reason for this are failures to identify synchronous sources at the 4th IT, instead finding single independent sources. A single-source at the 4th IT is generally located somewhere between the two actual

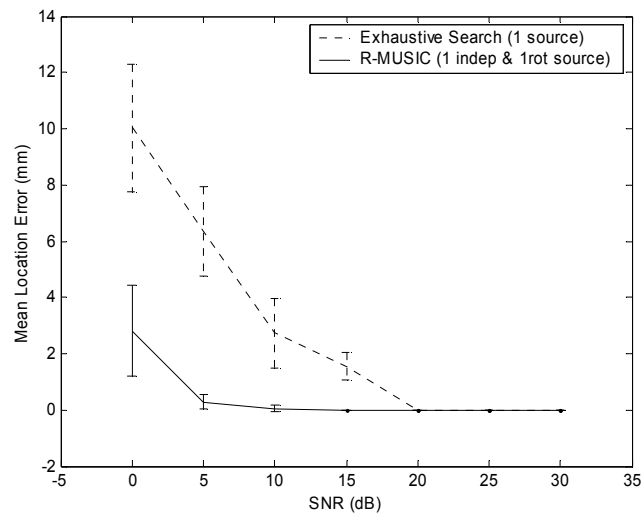


Figure 4.17 Localization error for 1 independent and 1 rotating source vs. best possible localization of a single source using spatial-only inverse for R-MUSIC.

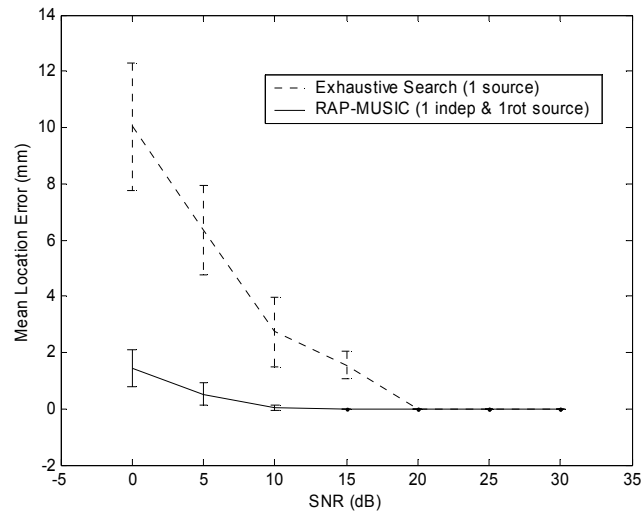


Figure 4.18 Localization error for 1 independent and 1 rotating source vs. best possible localization of a single source using spatial-only inverse for RAP-MUSIC.

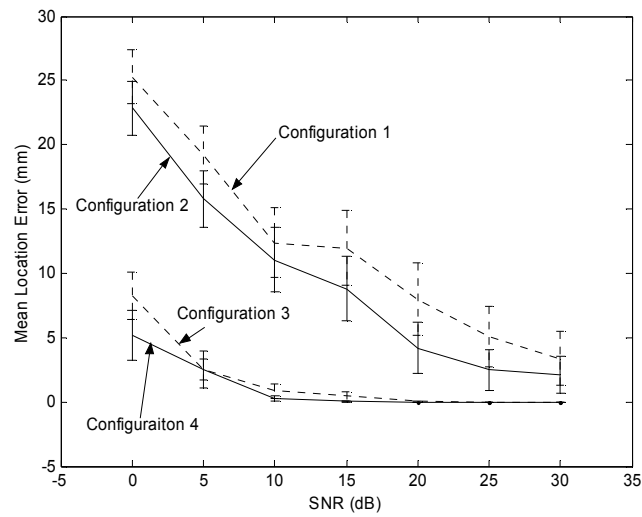


Figure 4.19 Localization error for source Configurations 1-4 using the empirical correlation threshold (see Eq. 4.3), generated using R-MUSIC.

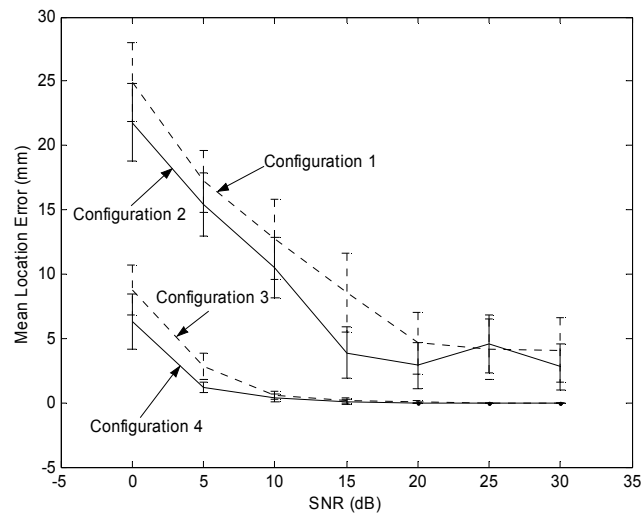


Figure 4.20 Localization error for source Configurations 1-4 using the empirical correlation threshold (see Eq. 4.3), generated using RAP-MUSIC.

synchronous sources. As the synchronous sources can be spatially disparate, a large location error will occur.

Figures 4.21-4.24 compare localization error for Configurations 1-4 for both algorithms. From these figures, it can be observed that the performance of the algorithms, R-MUSIC and RAP-MUSIC is statistically comparable. It was reported by Mosher *etal.* [10] that for two 1-dimensional asynchronous dipoles both algorithms perform the same at SNR 0 dB. These results are consistent with that finding, and extend it to a range of SNRs and complex configurations including synchronous sources with a variable correlation threshold.

Figures 4.25-4.32 compare the performance of R-MUSIC and RAP-MUSIC using the empirical correlation threshold in (4.3) with a fixed threshold of 0.95 as proposed by Mosher *etal.* [9]. As seen in Figures 4.25-4.26 and 4.29-2.30, using an empirical threshold significantly improves the performance of the algorithms for Configuration 1-2 above 15 dB as compared to using a fixed threshold of 0.95. For these two configurations, the performance below 15 dB is better using a fixed threshold of 0.95. The empirical threshold is clearly too low below 15 dB for these two configurations (Figures 4.9-4.10, 4.13-4.14) resulting in a poor performance. On the other hand, for Configuration 3-4 (Figures 4.27-4.28 and 4.31-4.32), the performance is similar using both the thresholds for SNRs above 15 dB. The performance is slightly better for Configuration 3 using an empirical threshold

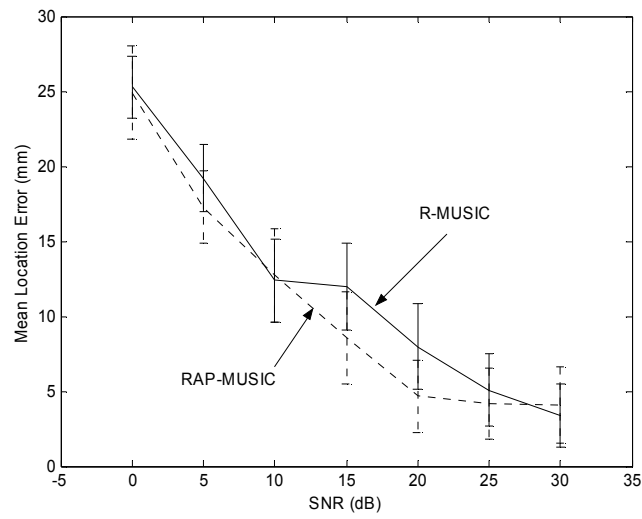


Figure 4.21 Localization error for source Configuration 1 using the empirical correlation threshold (Eq. 4.3) for R-MUSIC and RAP-MUSIC

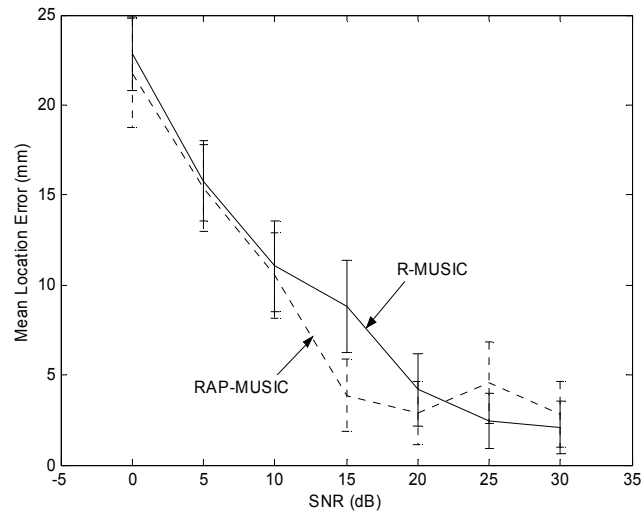


Figure 4.22 Localization error for source Configuration 2 using the empirical correlation threshold (Eq. 4.3) for R-MUSIC and RAP-MUSIC

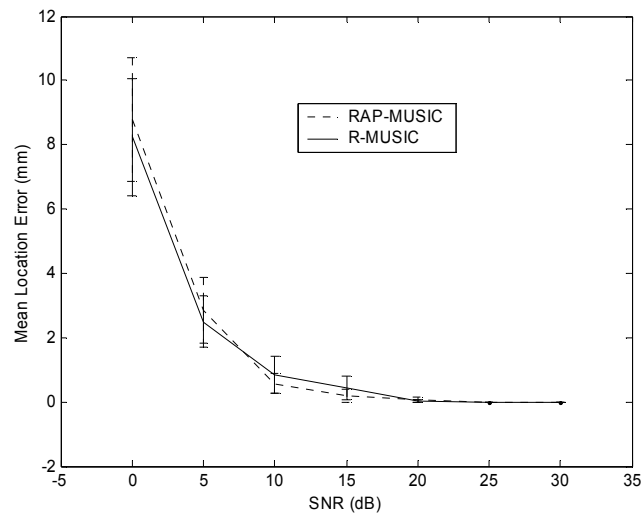


Figure 4.23 Localization error for source Configuration 3 using the empirical correlation threshold (Eq. 4.3) for R-MUSIC and RAP-MUSIC

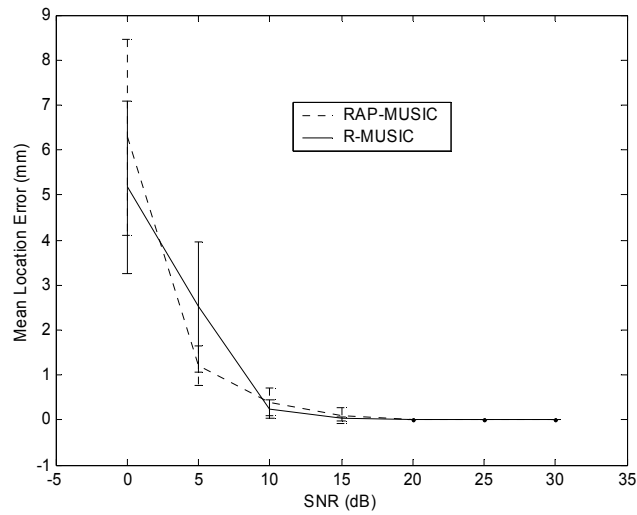


Figure 4.24 Localization error for source Configuration 4 using the empirical correlation threshold (Eq. 4.3) for R-MUSIC and RAP-MUSIC

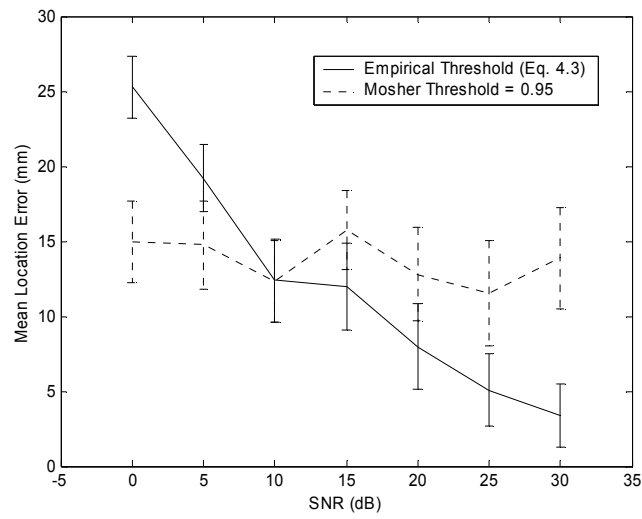


Figure 4.25 Localization error for source Configuration 1 generated using R-MUSIC.

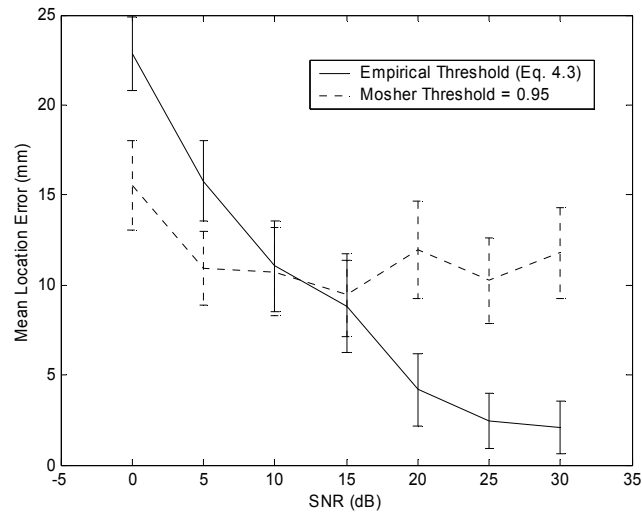


Figure 4.26 Localization error for source Configuration 2 generated using R-MUSIC.

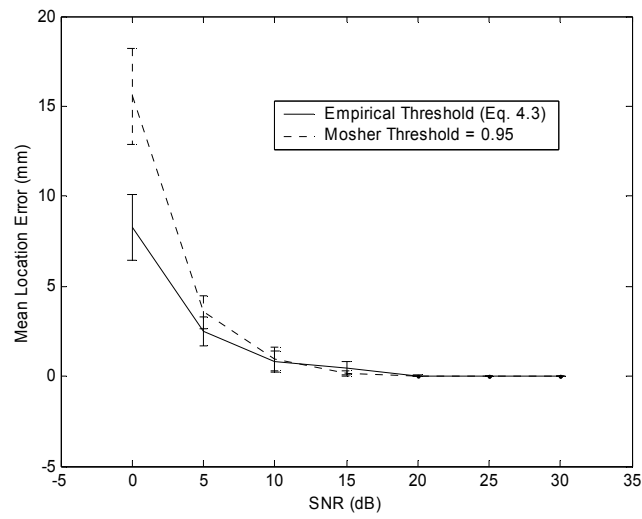


Figure 4.27 Localization error for source Configuration 3 generated using R-MUSIC.

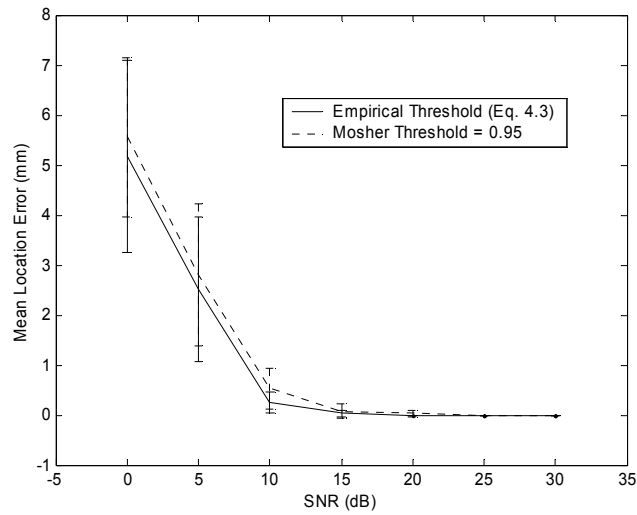


Figure 4.28 Localization error for source Configuration 4 generated using R-MUSIC.

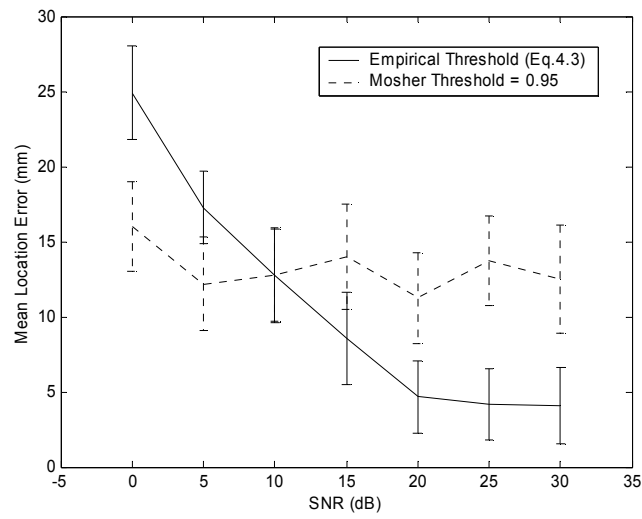


Figure 4.29 Localization error for source Configuration 1 generated using RAP-MUSIC.

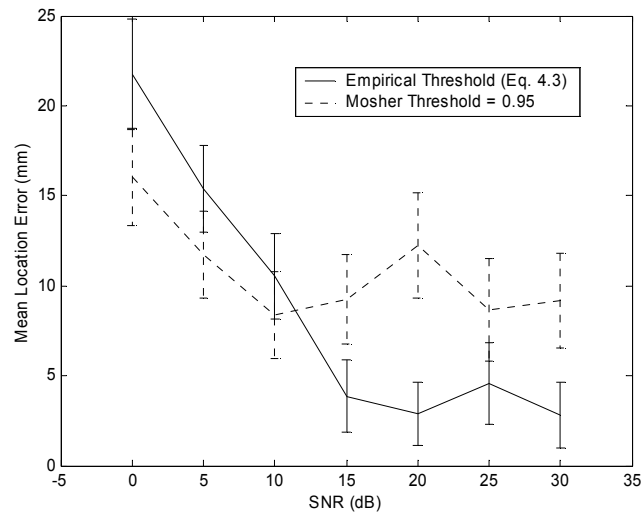


Figure 4.30 Localization error for source Configuration 2 generated using RAP-MUSIC.

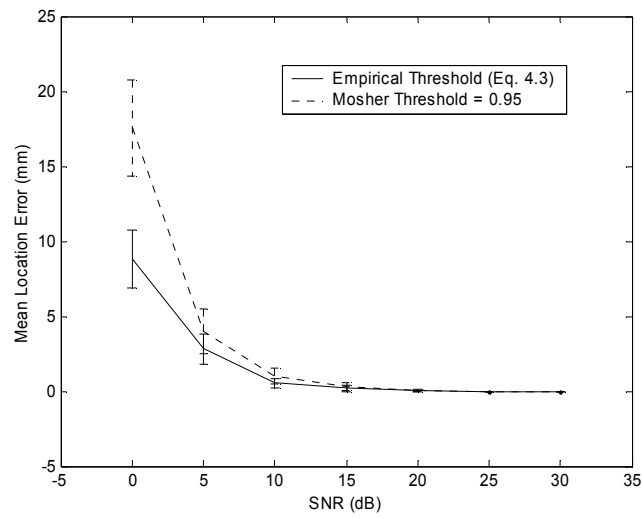


Figure 4.31 Localization error for source Configuration 3 generated using RAP-MUSIC.

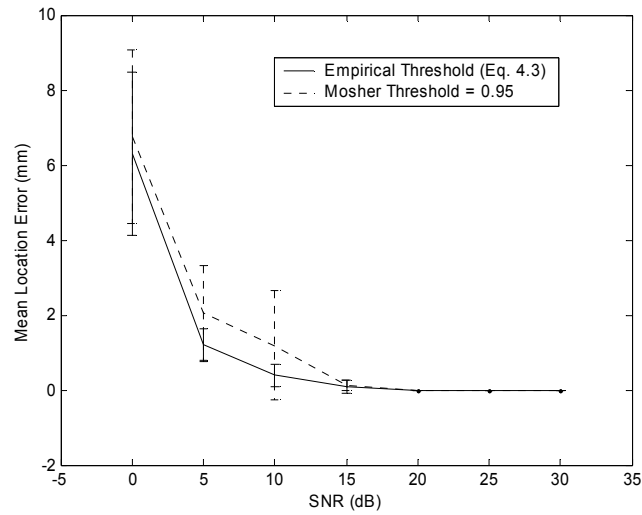


Figure 4.32 Localization error for source Configuration 4 generated using RAP-MUSIC.

for SNRs below 10 dB as 0.95 threshold is too high for this configuration (Figures 4.11, 4.15). These findings suggest that a threshold based on SNR is important to distinguish synchronous sources from asynchronous sources. The proposed empirical threshold works well for the configurations above 15 dB.

Although it was observed that a fixed correlation threshold is inadequate, these results indicate that the attempt to relate the threshold to estimated SNR is only partially successful. A robust distinction between synchronous and independent sources cannot be achieved by a simple choice of threshold. Reasonable performance, on the order of the cortical resolution, was obtained at higher SNRs.

The above results are for 0% correlated (independent) sources or 100% correlated (synchronous) sources. To see the effect of partially correlated time series on source localization, performance was measured for 2 sources of equal power at variable degree of correlation to each other. The empirical correlation threshold was used. The time series were composed by adding different sinusoidal time series. The cross correlation matrix, $\mathbf{R}_{\text{cross}}$, for the sources was specified as:

$$\mathbf{R}_{\text{cross}} = \begin{bmatrix} 1 & \gamma \\ \gamma & 1 \end{bmatrix} \quad (4.4)$$

where γ is the correlation coefficient matrix and determines the degree of correlation between the two sources. For this study, γ was chosen as 0, 0.2463, 0.5064, 0.7505 and 1.0.

The results for source localization are shown in Figures 4.33-4.34 for both algorithms. The performance of both algorithms is comparable. It can be seen that, as γ is increased, the localization error increases. The performance is very good for SNRs above 10 dB for partially correlated sources. The performance of synchronous sources is significantly degraded. Again, the analysis of the data shows that this is due to the failure to identify synchronous sources at the 2nd IT and instead a single independent source is found.

For partially correlated sources, the theory predicts a configuration comprising of 1-dipole IT and 2-dipoles IT. The analysis of the data shows that algorithms only identify two 1-dipole ITs, as the empirical threshold is not adequate for this source configuration. Still, the algorithms are able to identify the independent components of the two time series correctly. The results show that the correlation threshold is highly dependent on source configuration and probably on head model.

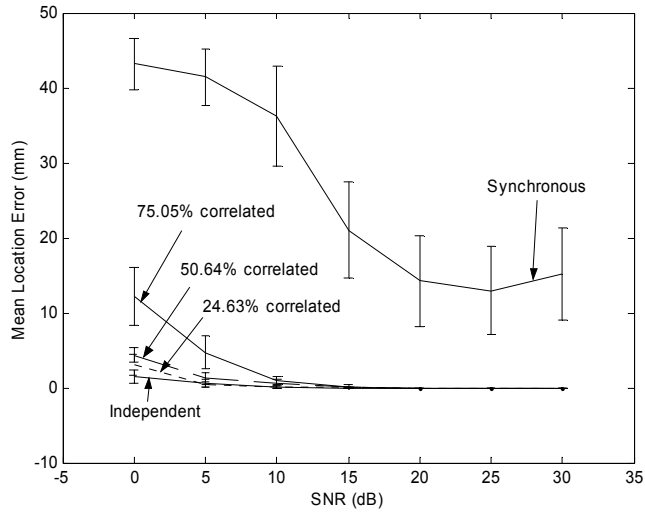


Figure 4.33 Localization error for two sources of equal power with 0%, 24.63%, 50.64%, 75.05 and 100% correlation generated using R-MUSIC.

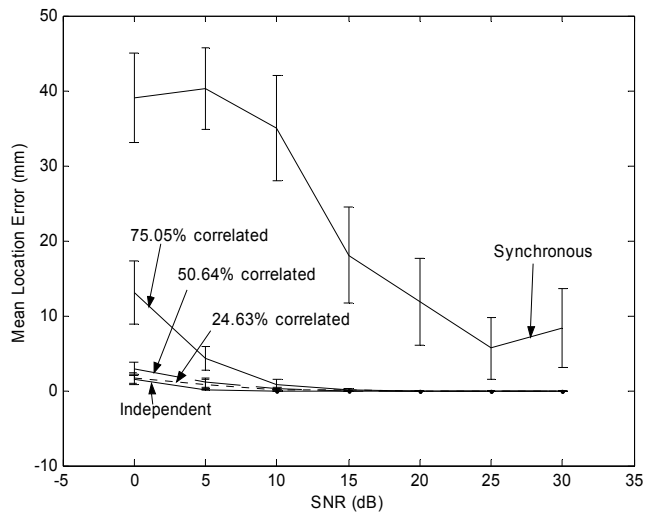


Figure 4.34 Localization error for two sources of equal power with 0%, 24.63%, 50.64%, 75.05% and 100% correlation generated using RAP-MUSIC.

Chapter 5

CONCLUSIONS

In this work, a study of localization performance of cortical sources in a realistic human head model has been performed. Signal subspace methods, R-MUSIC and RAP-MUSIC, were used to simulate various rank-four source configurations for SNRs 0 to 30 dB. The main conclusions of this study have been summarized in this chapter.

This study shows that a spatio-temporal treatment can dramatically improve localization performance over a spatial-only analysis, at least for sources with mutually independent temporal signals. For algorithms based on the scanning of independent source topographies, a critical factor is the decision process for determining whether the next source topography contains multiple synchronized sources. The problem of distinguishing synchronous sources from asynchronous sources is not simple. Using a fixed threshold to treat configurations containing synchronous pair is inadequate. A simple threshold based on SNR gives improved performance over a fixed threshold for higher SNRs. However, this attempt is only partially successful. Localization for configurations containing

synchronous sources was substantially degraded at signal-to-noise ratios below 20 dB and for the whole range of SNR for a pair of synchronous sources. The problem of identifying synchronous sources is more critical and improved methods are needed to distinguish between asynchronous and synchronous sources.

For a pair of partially correlated sources, algorithms identify two independent sources, instead of finding one independent source and a pair of synchronous sources. This is again the issue of identification of synchronous sources and establishing the correct correlation threshold. Still algorithms are able to identify the independent portion of the time series and source localization is very good above 10 dB. Therefore, algorithms can be successfully used for source localization of partially correlated sources above 10 dB.

The performances of both the algorithms, R-MUSIC and RAP-MUSIC, were comparable to each other. The computational complexity of the multidimensional search was successfully reduced by initializing the multi-dimensional search with the results of a lower-resolution search, and locally constraining the search region.

REFERENCES

- [1] P. L. Nunez, "Localization of brain activity with electroencephalography," *Advances in Neurology*, vol. 54, pp. 39-65, 1990.
- [2] S. K. Law and P. L. Nunez, "Quantitative representation of the upper surface of the human head," *Brain Topogr.*, vol. 3, pp. 365-371, 1991.
- [3] S. K. Law, "Thickness and resistivity variations over the upper surface of the human skull," *Brain Topogr.*, vol. 6, pp. 99-109, 1993.
- [4] P. H. Schimpf, C. Ramon and J. Haueisen, "Dipole models for the EEG and MEG," *IEEE Trans. Biomed. Eng.*, vol. 49, pp.409-418, 2002.
- [5] C. C. Wood, "Application of dipole localization methods to source identification of human evoked potentials," *Ann. New York Acad. Sci.*, vol. 388, pp. 139-155, 1982.
- [6] M. Scherg and D. von Cramon, "Two bilateral sources of the late AEP as identified by a spatio-temporal dipole model," *Electroencephalogr. Clin. Neurophysiol.*, vol. 62, pp. 32-44, 1985.
- [7] R. O. Schmidt, "Multiple emitter location and signal parameter estimation," *IEEE Trans Antennas Propag.*, vol. AP-34, pp. 276-280, 1986.
- [8] J. C. Mosher, P. S. Lewis and R. M. Leahy, "Multiple dipole modeling and localization from spatio-temporal MEG data," *IEEE Trans. Biomed. Eng.*, vol. 39, pp. 541-557, 1992.
- [9] J. C. Mosher and R. M. Leahy, "Recursively applied MUSIC: A framework for EEG and MEG source localization," *IEEE Trans. Biomed. Eng.*, vol. 45, pp. 1342-1354, 1998.
- [10] J. C. Mosher and R. M. Leahy, "Source localization using Recursively Applied and Projected (RAP) MUSIC," *IEEE Trans. Signal Processing*, vol. 47, pp. 332-340, 1999.
- [11] P. L. Nunez, *Electric fields of the brain: The neurophysics of EEG*, Oxford University Press, New York, 1981.

- [12] W. Chen and K. M. Wong, "Detection of the number of signals: A predicted eigen-threshold approach," *IEEE Trans on Signal Processing*, vol. 39, pp. 1088-1098, 1991.
- [13] J. Wang, S. J. Williamson and L. Kaufman, "Magnetic source images determined by a lead-field analysis: the unique minimum-norm least squares estimation," *IEEE Trans. Biomed. Eng.*, vol. 39, pp. 665-675, 1992.
- [14] M. Huang, C. J. Aine, S. Supek, E. Best, D. Ranken and E. R. Flynn, "Multi-start downhill simplex method for spatio-temporal source localization in magnetoencephalography," *Electroencephalogr., Clin. Neurophysiol.*, vol. 108, pp. 32-44, 1998.
- [15] P. Schimpf, J. Haueisen, C. Ramon, and H. Nowak, "Realistic computer modeling of electric and magnetic fields of human head and torso," *Parallel Computing*, vol. 24, pp. 1433-1460, 1998.
- [16] N. Shrinidhi, D. R. Haynor, Y. Wang, D. B. Joregenson, G. H. Bardy, and Y. Kim, "An efficient tissue classifier for building patient-specific finite element models from X-ray CT images," *IEEE Trans Biomed Eng*, vol. 43, pp. 333-337, 1996.
- [17] P. H. Schimpf, J. Haueisen, and C. Ramon, "Ellipsoidal refinement of the regularized inverse: performance in an anatomically realistic EEG model," *IEEE Tran Biomed Eng*, vol. 51, No. 4, pp. 679-683, 2004.